Trans. Japan Soc. Aero. Space Sci.
Vol. 65, No. 1, pp. 23–32, 2022
DOI: 10.2322/tjsass.65.23

Modified Lifting Line Method Based on Vortex Rings and Its Application on Lift Fan Design*

Haitong WANG,[1)] Yangang WANG,[1)†] Siwei WANG,[1)] Fang ZHOU,[1)] and Hanru LIU[1),2)]

[1)]*School of Power and Energy, Northwestern Polytechnical University, Xi'an, Shaanxi 710129, China*
[2)]*Research & Development Institute in Shenzhen, Northwestern Polytechnical University, Shenzhen, Guangdong 518057, China*

The image vortex model is widely used in lifting line method to predict the flow induced by the shroud and hub surface in ducted fan, but it does not perform well in lift fan design due to the zero far field inflow. In this paper the theoretical defects and numerical error propagation characteristic of the image vortex model in simulating duct surface are studied. Then the vortex rings correction based on image vortex model is verified and applied in lifting line method. In order to test the improved method, a 150 mm diameter lift fan is designed by the modified lifting line method, after that, analyzed by the modified lifting line itself and RANS solver respectively. The results show that the contribution of the vortex rings at the rotor accounts for 50% of the total induced velocity, and it accounts for 35% at the stator, which verifies the necessity of the vortex rings correction. The performance of the rotor and stator geometry is consistent with the design expectation, the efficiency is up to 90.97% by numerical simulation and 88.32% by experimental measurement, which confirms the reliability of the modified lifting line method developed in this paper especially on lift fan design.

Key Words: Lifting Line Method, Vortex Ring, Lift Fan, V/STOL

1. Introduction

Over the past decades, vertical take-off and landing aircraft has been widely used in many fields and has great potential for future Urban Air Mobility (UAM),[1)] which promote urgent requirement of more safety and higher efficiency propulsion systems. The lift fan can produce more lift than the propeller with the same power input and blade diameter, and has no exposed rotating parts, which can effectively prevent the blades from damaging the surrounding environment and itself.[2,3)] Furthermore, the shroud is expected to reduce the noise propagation and suppress the tip vortex at the same time. Compared with other lift systems, lift fans will play an increasingly important role in urban aviation, low-speed aviation, and drones.[4)]

The lift fan can be seen as a special ducted fan that enables the aircraft to hover which has been extensively studied by researchers.[5,6)] With the further understanding of the flow characteristics of ducted fan/propeller, the design theory and method are becoming more accurate and efficient. Among them, the lifting line method based on inviscid and incompressible assumption is a very effective design method for subsonic fluid machinery.[7)] The classical lifting line method treats the blade as bound vortices with a specific intensity distribution and the helical wake vortex filaments shed from the endpoints of bound vortices.[8)] Hsin[9)] compared several methods to calculate the self-induced velocity of the bound vortex and the wake vortex. It was concluded that the Lerbs'[10)] and Wrench's[11,12)] methods have the best accuracy and efficiency, and Hough and Ordway's[13,14)] method is considered to have a good performance in the process of solving the interference-induced velocity between rotor and stator. Those methods have been applied in the research of Epps[15)] and had good results.

The classical lifting line method has been successfully applied to propeller design, but how to predict the additional aerodynamic effect brought by the duct surface effectively and accurately is still an important problem in the design of ducted fan. To calculate the interaction between duct and propeller, Dickmann et al.[16)] considered the ducted propeller as a propulsion unit and described the duct using momentum theory. XROTOR[17)] uses the equivalent propeller concept to model the additional induction from a duct. But these two methods mentioned above are not accurate enough. Caster[18)] combined the Lerbs'[10)] moderately loaded propeller theory with the linearized theory of duct[19)] to iteratively calculate the interaction between the duct and the propeller. However, it also did not include the circumferential velocity induced by the duct. Similarly, DFDC (Ducted Fan Design Code)[20)] was based on axisymmetric panel representation of the duct, but the tangential induced velocity was given directly in terms of the local circulation of all upstream blade rows. In order to calculate circumferential induced velocity generated by duct, Kerwin et al.[21,22)] used the image vortex method to simulate the duct effect. This method was not derived theoretically, but could be proved effective by some numerical calculations and was widely used.[23)] To calculate the axial and circumferential induced velocity of the duct at the same time, Houten[24)] developed a ducted propeller analysis program DPSF (Ducted Propeller in Steady Flow). This program used vortex lattices to represent the ducted propeller and the thickness was represented by line sources at the same

© 2022 The Japan Society for Aeronautical and Space Sciences
*Received 8 February 2021; final revision received 9 June 2021; accepted for publication 19 July 2021.
†Corresponding author, wyg704@nwpu.edu.cn

location as the vortices, but the demand for computing resources was relatively high. Coney[25] compared the induced velocity distributions for a ducted propeller between the panel method and the image vortex method. In this case the advance coefficient was 1.143, with uniform inflow coming to the duct. Result showed a good agreement between the two models. Coney also pointed out that the image vortex method is a more effective and accurate method to deal with the duct effect. However, the above methods were verified in ducted fans which were working in cruise conditions, it still lacks of test for the design capability of lift fan which mainly works in hovering condition. In previous research on lift fans, it is found that the aerodynamic effect of duct cannot be accurately simulated only by using the image vortex model.[26]

Therefore, the purpose of this paper is to expand the application of lifting line method in the field of ducted fan design, so that it can be used in the design of ducted fan with zero inflow speed, such as lift fan. Firstly, based on previous research, an error introduced by the image vortex when encountering parallel walls, such as hub and shroud, and its propagation characteristics in the design process are analyzed. Secondly, the parallel wall problem is processed under two-dimensional conditions. Based on the image vortex method, the error correction is performed using the vortex rings, and the compatibility between the image vortex and the vortex rings is verified. At last, the vortex rings correction for the hub and shroud effect of the ducted fan in the three-dimensional environment is established, and the 150 mm diameter lift fan is taken as an example for numerical verification.

2. Error Analysis

2.1. The error of the single-layer image vortex

One of the most important function of the lifting line method in the design process is to obtain the axial and tangential velocity at the bound vortices. The induced velocity comes from the horseshoe vortex system which consists of bound vortex and wake vortex induced by blades, hub and shroud. In the traditional method, two layers of image vortex are arranged inside the hub and outside the shroud respectively for all horseshoe vortices in the passage to simulate the effect of the parallel wall, as shown in Fig. 1.

The method of single image vortex is not accurate enough to predict the induced velocity. This is because that the Neumann boundary condition cannot be realized by using a single-layer image vortex for each wall when there are two parallel walls. The image vortex of image vortex still needs to be calculated, which means that we need infinite image vortex to realize the Neumann boundary conditions.[27]

To further discuss this phenomenon, two-dimensional vortex model is taken as an example in Fig. 2. Assume that there is a pair of parallel walls with a length of $10d$, a spacing of $1d$, and a point vortex with unit strength in the center. To simulate the wall effect, the first layer image vortex is arranged at $y = \pm d$, the second layer image vortex which is

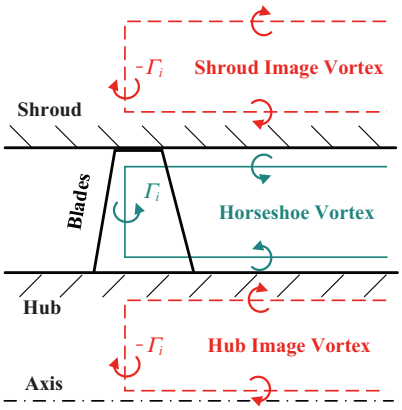


Fig. 1. Image vortex of horseshoe vortex between parallel walls.

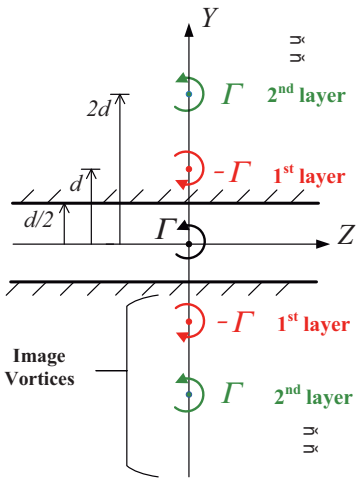


Fig. 2. Image of point vortex between parallel walls.

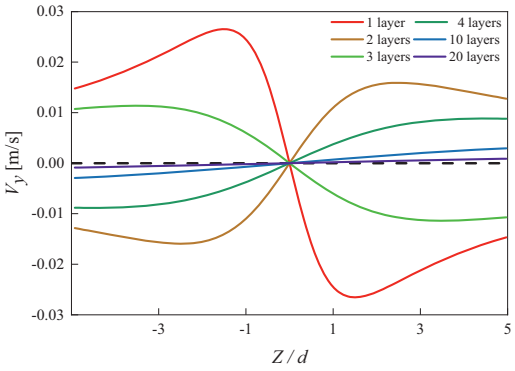


Fig. 3. Induced normal velocity on the upper wall.

the image vortex of the first layer image vortex is arranged at $y = \pm 2d$, and so on.

Figure 3 shows the total normal induced velocity of the point vortex and the image vortex of different layers on the upper wall. When there is only a single-layer image vortex, the normal velocity of the wall surface is high, which means it cannot realize the wall boundary condition accurately. The reason is that the single image vortex might eliminate the normal induced velocity on its wall and induce a new normal velocity on the parallel wall at the same time. With increas-

©2022 JSASS

ing the number of layers of the image vortex, the normal induced velocity is eliminated by the image vortex far away from the wall. Finally, the wall-normal velocity converges to zero gradually.

The Z-direction induced velocity which is generated by the image vortex of different layers at the monitoring line is extracted, and the monitoring line is set at $z = 0.0d$, $y = 0.00$–$0.4d$. The results are shown in Fig. 4. For parallel walls if there is only a single layer of image vortex being used to simulate the wall effect, a low-accuracy result which is not convergent is obtained.

In the design of the ducted fan with high cruising speed, this low precision result will not have a serious impact due to the propagation of errors. But it is fully exposed to the design of the lift fan, especially there is zero inflow. Additional model must be added to correct this result.

2.2. Error propagation of induced velocity

To illustrate the error propagation process, V_z can be defined as the total axial induced velocity in the duct, composed of V_{in} and u_a, where V_{in} is the free inflow velocity, and u_a is the axial induced velocity. According to the relative error transfer formula, relative error of V_z can be derived as shown in Eq. (1). It can be seen that the relative error $\Delta u_a/u_a$ has an increasing influence on the total axial induced velocity with the decreasing of the inflow velocity. When the inflow velocity is zero, this error will be directly propagated to the total axial velocity.

$$\frac{\Delta V_Z}{V_Z} = \frac{1}{\dfrac{V_{in}}{u_a} + 1} \frac{\Delta u_a}{u_a} \tag{1}$$

Similarly, Eq. (2) describes the relationship of the error of the circumferential induced velocity between other parameters in the duct. V_θ is the total circumferential relative velocity, ω is the rotational angular velocity, r is the local radius, and u_θ is the circumferential induced velocity. It is obvious that the error of the circumferential induced velocity does not significantly affect the error of the total circumferential relative velocity because u_θ is a small value compared to $\omega \cdot r$.

$$\frac{\Delta V_\theta}{V_\theta} = \frac{1}{\dfrac{\omega \cdot r}{u_\theta} + 1} \frac{\Delta u_\theta}{u_\theta} \tag{2}$$

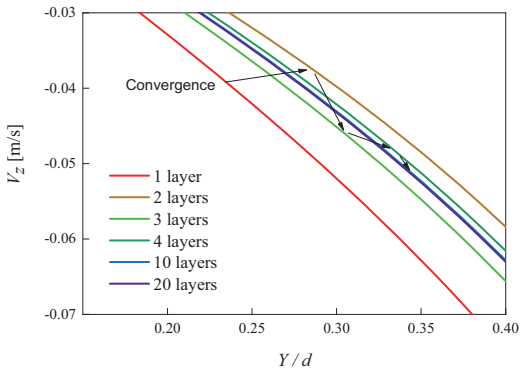


Fig. 4. Induced velocity in Z-direction.

Based on the analysis of the error propagation discussed in the previous paragraph, we can say that the calculation accuracy of axial induced velocity is the key shortcoming that limits the application of the lifting line method when it was used in the low-speed propulsion units such as lift fans with $V_{in} = 0\,\mathrm{m/s}$. If it is not correct, the lifting line method will produce a completely wrong blade geometry in this situation.

3. Vortex Rings Correction Method

To achieve an accurate result in the lifting line method, each vortex in the passage needs an image vortex to be constructed with enough layers. As the increasing of stage number of ducted fan or the discretization of the lifting line becomes finer, it will consume more computing resources because of more image vortices. Therefore, it is more suitable to use vortex rings instead of the multi-layer image vortices system except the first layer to simulate the wall effect.

3.1. Two-dimensional verification of vortex rings correction

Based on the single-layer vortex model, as shown in Fig. 2, the wall effect is modified by the vortex rings to obtain the reasonable wall-normal induced velocity and high-precision axial induced velocity. First of all, the two-dimensional problems which are simplified from the three-dimensional problems is taken for preliminary verification, and the vortex model is shown in Fig. 5. Different from Fig. 2, only the first layer of image vortex is retained in this model, and several vortices of unknown strength are arranged along the parallel wall. It should be noted that each vortex ring degenerates into a point vortex from three-dimensional environment to two-dimensional environment. But it is still called the vortex ring in this paper for the sake of the unity of description.

In this method, the first step is to construct a linear equation to calculate the circulation distribution of vortex rings on

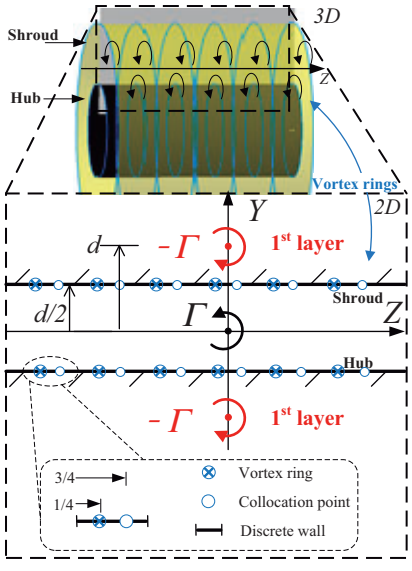


Fig. 5. Vortex ring correction model for parallel walls.

©2022 JSASS

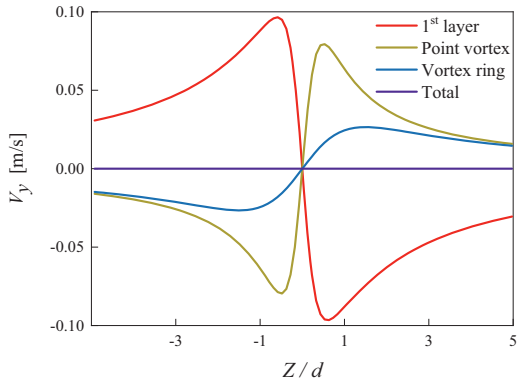


Fig. 6. Induced normal velocity on the upper wall.

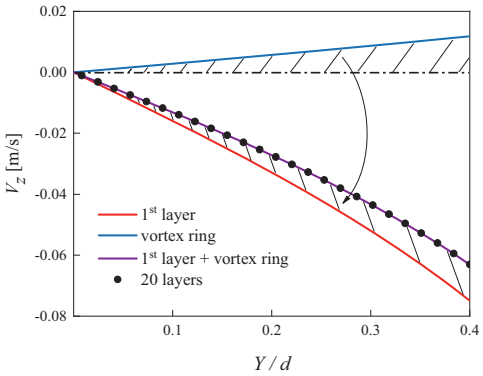


Fig. 7. Induced velocity in Z-direction.

the wall, as shown in Eq. (3). Firstly, the normal induced velocity of point vortex and two image vortices at the control points of each wall are calculated to form the right-hand-side matrix (RHS), as shown in Eq. (4). Then the induced coefficient matrix A is constructed according to the induced coefficients of each vortex ring, as shown in Eq. (5). Finally, the circulation distribution Γ of each vortex on the wall is obtained by solving the linear equations.

$$\sum_{j=1}^{N} A_{ij}\Gamma_j = RHS_i \tag{3}$$

$$RHS_i = \frac{-\Gamma}{2\pi}\frac{z_i}{(z_i)^2+(y_i)^2} + \sum\frac{\Gamma}{2\pi}\frac{z_i - z_{\text{image}}}{(z_i - z_{\text{image}})^2+(y_i - y_{\text{image}})^2} \tag{4}$$

$$A_{ij} = \frac{-1}{2\pi}\frac{z_i - z_j}{(z_i - z_j)^2+(y_i - y_j)^2} \tag{5}$$

Where i is the control point index number and j is the vortex rings index number.

Figure 6 shows the contribution of each element to the normal induced velocity on the upper wall. The point vortex locates in the center of the model, so the normal induced velocity is symmetrical about the center. The trend of the velocity induced by the first layer of image vortex is opposite to that of the point vortex, but the value is higher. It can be known from Eq. (3) that the vortex rings corrected this deviation, which could make sure that the total normal induced velocity of the wall is strictly zero.

To determine the effectiveness of the method, Fig. 7 shows the Z-direction induced velocity profile induced by the parallel wall. The results of the first 20 layers of image vortices are regarded as convergence results that meet the accuracy requirements. Obviously, the 1st layer image vortex cannot accurately describe the induced effect of the parallel wall, and the predicted velocity distribution V_z is much lower than the convergence results. However, if the positive correction to the V_z velocity of the vortex ring is superimposed on the 1st layer image vortex, that is, the shaded part in the figure, the velocity distribution is exactly consistent with the convergence results.

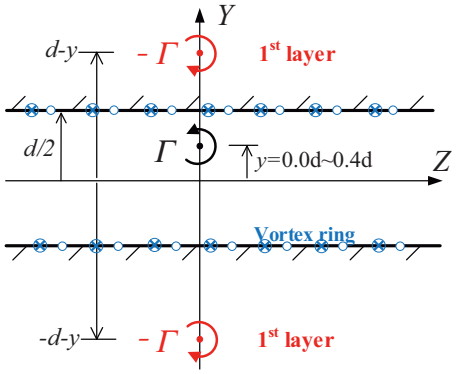


Fig. 8. The calculation model of point vortex at the noncentral position.

These studies indicate that the vortex ring method is compatible with the image vortex method. The vortex rings successfully replaced all the image vortices except the first layer. The induced effect of the parallel walls on the velocity field is simulated accurately. However, this point vortex is located at the center of the parallel wall, so it is necessary to further confirm the universality of the method.

Based on the model in Fig. 5, the position of point vortex is moved along the Y-direction from 0.0 to 0.4d as shown in Fig. 8. The position of the vortex rings remains unchanged and the distribution of the circulation is calculated again. The position of the first layer image vortex changes with the change of y, where the upper wall image vortex is located at $y = d - y$ and the lower wall image vortex is located at $y = -d - y$.

Figure 9 shows the normally induced velocity of point vortex, its first image vortex and vortex rings on the upper and lower wall surfaces. The normal induced velocity of the first layer image vortex and the vortex rings are added with a minus sign to facilitate comparison. When the point vortex is located at the center $y = 0$, the induced velocity distribution of the point vortex to the upper walls is same as the lower walls. As the point vortex approaches the upper wall, the normal induced velocity of the point vortex to the upper wall increases and the normal induced velocity to the lower wall decreases. However, no matter where the point vortex locates, the wall boundary conditions can be realized accurately.

©2022 JSASS

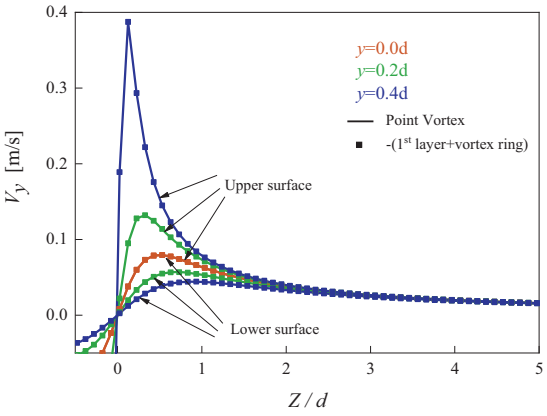


Fig. 9. Normal induced velocity at upper and lower wall.

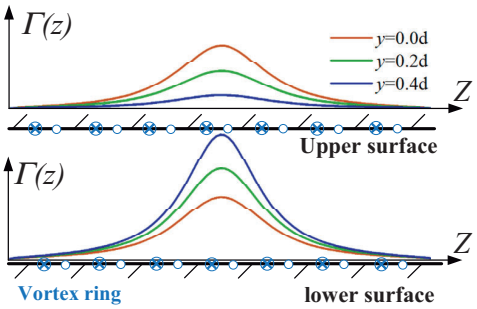


Fig. 10. The distribution of vortex ring circulation in Z-direction.

The circulation distribution of the upper and lower wall vortices is shown in Fig. 10. When the point vortex is in the center, the circulation distribution of the vortex rings is the same on the upper and lower wall. When the point vortex is close to the upper wall, the lower wall image vortex will be far away from the upper wall and produce less normal induced velocity. Therefore, the upper wall vortex rings with lower intensity can correct the normal induced velocity.

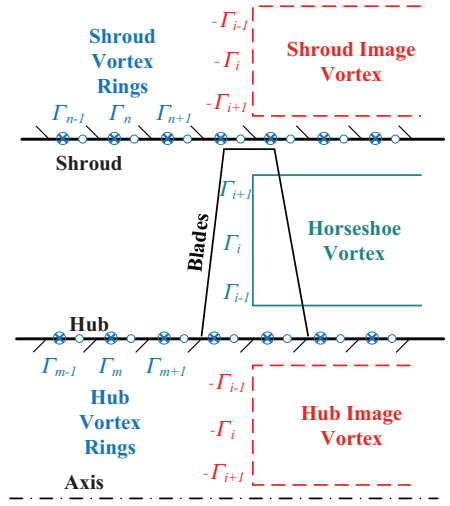


Fig. 11. Lifting line method with vortex rings correction.

The lower wall needs to be modified by stronger vortex rings.

3.2. Application of vortex ring in lifting line method

The processing of three-dimensional flow is similar to that of two-dimensional problems. Based on the single-layer image vortices, the vortex rings are added to further eliminate the radial velocity on the wall that should not exist. Taking the lifting line design of a single rotor as an example, a model is established as shown in Fig. 11.

The hub and shroud are assumed to be cylindrical surfaces extending upstream and downstream. For any horseshoe vortex, single-layer image vortex $-\Gamma_i$ is added to the hub and the shroud. Then the vortex ring Γ_m and Γ_n are arranged. To obtain the strength of the vortex rings, the hub and the shroud are divided into several equally spaced segments, and the vortex rings are arranged at one-quarter of the axial direction of each segment, and the collocation points are arranged at three quarters. The following linear equations are established:

$$\begin{pmatrix} A_{11} & \cdots & A_{n1} & A_{(n+1)1} & \cdots & A_{(n+m)1} \\ \vdots & \ddots & \vdots & \vdots & \ddots & \vdots \\ A_{1n} & \cdots & A_{nn} & A_{(n+1)n} & \cdots & A_{(n+m)n} \\ A_{1(n+1)} & \cdots & A_{n(n+1)} & A_{(n+1)(n+1)} & \cdots & A_{(n+m)(n+1)} \\ \vdots & \ddots & \vdots & \vdots & \ddots & \vdots \\ A_{1(n+m)} & \cdots & A_{n(n+m)} & A_{(n+1)(n+m)} & \cdots & A_{(n+m)(n+m)} \end{pmatrix} \begin{pmatrix} \Gamma_1 \\ \vdots \\ \Gamma_n \\ \Gamma_{n+1} \\ \vdots \\ \Gamma_{n+m} \end{pmatrix} = - \begin{pmatrix} RHS_1 \\ \vdots \\ RHS_n \\ RHS_{n+1} \\ \vdots \\ RHS_{n+m} \end{pmatrix} \tag{6}$$

Where A is the induced coefficient of each vortex ring to collocation points, can be calculate by formulas given by Kuchemann and Weber.[28] The subscripts n and m are index corresponding to the shroud and hub vortex rings respectively. RHS is the sum of the radial induced velocity of the singular elements which are horseshoe vortices and image vortices in collocation points, can be calculate by formulas given by Wrench and Hough in references.[11–14] By solving the $(m+n)\cdot(m+n)$ dimensional linear equations, the circulation distribution of the vortex rings in the hub and the shroud is calculated. Finally, the induced velocity of vortex rings to the bound vortex is obtained, and the accurate total induced velocity is achieved by superposition with velocity induced from other sources.

From the perspective of potential flow, the construction of the non-constricted duct flow at the blade disk is further description in Fig. 12. Compared with the ducted flow constructed by the lifting line method combined with the image

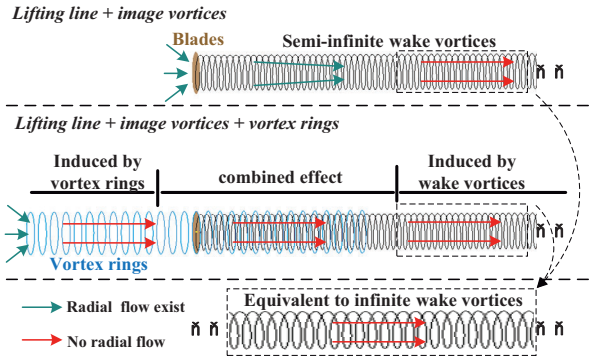


Fig. 12. Potential flow field induced by different methods.

vortex, due to the incomplete elimination of the radial velocity, the flow structure at the blade disk is still similar to the constricted flow induced by the blade's semi-infinite wake vortex. Until the downstream flow is far away from the blades, the downstream flow structure is approximately induced by the infinite wake vortex, and then the radial flow disappears. When the vortex rings are added, the contraction effect of the semi-infinite wake vortex should be automatically corrected by the vortex rings, and a non-contraction flow structure of the ducted fan in the long tube will be successfully constructed. In order to achieve this, the vortex rings need to be arranged long enough. The start point of vortex rings should be far enough from the semi-infinite wake vortex, to ensure the flow is mainly induced by the vortex rings and the end point of vortex rings should overlap with semi-infinite wake vortex, until the wake vortex fully developed in the downstream. At this time the flow in the downstream where is far from the vortex rings, the flow is mainly induced by the fully developed semi-infinite wake vortex, and because of the sufficient distance from the blade disk, it can be regarded as the ducted flow induced by the infinite wake vortex. And the flow near the blade disk is jointly induced by the semi-infinite wake vortex and the vortex rings, and the radial velocity is automatically corrected by the vortex rings to obtain a reasonable flow structure. To make the picture clear, only the principal diagram is drawn in Fig. 12 and the image vortex is omitted. This method will be used in the next section with an example to strengthen the confidence of users.

In addition, for the ducted fan with rotor and stator row, only horseshoe vortex and single-layer image vortex of stator need to be added to the model in Fig. 11, without adding more vortex rings. In the same way, this method can be used for the design of contra-rotating fans and multistage fans. The design process of lifting line with the vortex rings correction can be summarized in Fig. 13.

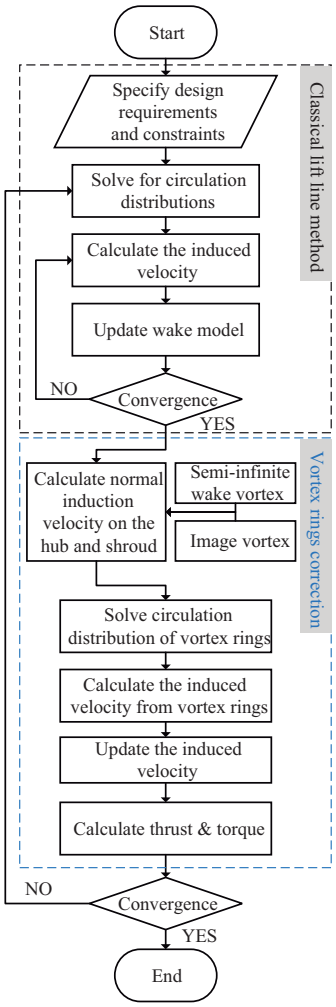


Fig. 13. Flow chart for lifting line method with vortex rings correction.

Table 1. Target parameters.

Parameters	Value
Thrust (N)	20.0
Torque ratio (R1/S1)	1:1
Rotational speed (RPM)	11000

Table 2. Geometric parameters.

Parameters	Value
Shroud diameter (mm)	150
Hub diameter (mm)	60
Number of rotor blades	10
Number of stator blades	6
R1 root chord length (mm)	35
R1 tip chord length (mm)	25
S1 root chord length (mm)	55
S1 tip chord length (mm)	55

4. Application and Verification of Developed Lifting Line Method

4.1. Example of lift fan design

Based on the developed lifting line method, a lift fan is designed for the vertical takeoff and landing vehicle with distributed propulsions. The target and geometric parameters are shown in Tables 1 and 2.

The rotor (R1) and the stator (S1) are divided into 10 segments equally along the radial direction. It means there are 100 horseshoe vortices in the rotor and 60 horseshoe vortices in the stator. The start point and the end point of the vortex rings are sited at 13 times of the rotor radius length from

©2022 JSASS

the rotor to the upstream and downstream respectively. For the case in this paper, the reason for selecting 13 times of the rotor radius is that at 13 times radius upstream, the influence of semi-infinite wake vortex is nearly disappeared, and symmetrically at the 13 times radius downstream, the semi-infinite wake vortex is close to the infinite horseshoe vortex model, which means horseshoe vortex itself does not induce radial induced velocity any more. So, no more vortex rings are needed. Since the load of each blade is the same, only one blade of the rotor and stator is taken as the representative respectively to design the radial circulation distribution. To achieve uniform velocity distribution at the outlet, equal circulation distribution is adopted for both the rotor and the stator, as shown in Eqs. (7) and (9). Next, the ratio of *const1* and *const2* should be determined to balance the torque of R1 and S1. Since the force direction of the lifting line is always perpendicular to the direction of the incoming flow. It can be seen from the velocity triangle that the torque of the lifting line comes from the axial component of the relative incoming flow, and the thrust comes from the circumferential component of the relative incoming flow. Then it is further considered that the axial velocity in the duct is equally distributed and constant under the assumption of time-averaged, non-viscosity and incompressibility. So, the ratio between the *const1* and *const2* should be exactly the inverse ratio of the number of blades.

$$\Gamma_{\text{R1-blade1}} = \Gamma_{\text{R1-blade2}} = \cdots\cdots = \Gamma_{\text{R1-blade10}} = const1 \quad (7)$$

$$\Gamma_{\text{S1-blade1}} = \Gamma_{\text{S1-blade2}} = \cdots\cdots = \Gamma_{\text{S1-blade6}} = const2 \quad (8)$$

$$\Gamma_{\text{R1}}/\Gamma_{\text{S1}} = 10/6 \quad (9)$$

To achieve the design goal of total thrust 20 N, there is only one unknown variable (Γ_{R1} or Γ_{S1}) Based on the Eqs. (7) to (9), the required circulation distribution can be obtained through iteration.

The rest parameters such as relative inflow velocity, angle of attack and lift at the bound vortex of the rotor and stator can be calculated as same as classical lifting line method.[29] The chord length has been given by design constraints. Therefore, the lift coefficient of the profile corresponding to each blade segment can be calculated. The three-dimensional geometry of the rotor and stator of the lift fan is constructed by the thin-airfoil theory. In this case, the rotor and stator blades use the parabolic chamber and NACA 00xx thickness distribution law as the design reference. Final results are shown in Fig. 14. And in terms of computing resources, although the time cost of the vortex ring is basically the same as a layer of image vortex, the vortex ring avoids the calculation of more layers of image vortex. It can be seen that the vortex ring is a highly efficient calculation method.

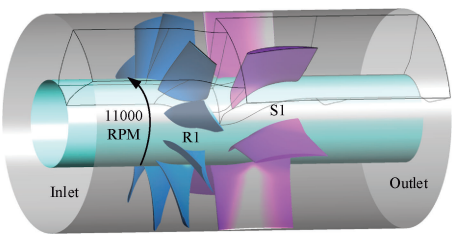


Fig. 14. 3D geometry of the lift fan blades.

4.2. Validation of developed design method

Three-dimensional geometry is calculated by CFX based on the RANS equations of compressible fluid to further confirm the design method. The total pressure and temperature at the inlet are 101325 Pa and 300 K respectively, and the average static pressure at the outlet is 101325 Pa. No-slip boundary condition is adopted on the wall. The stage interface is used between the rotor and stator to obtain the time-average performance. The single passage is used, and the periodically structured grid is used to discretize the space around the rotor and stator blade respectively. The tip clearance of the rotor is set to 0.5 mm, and SST turbulence model is used. To ensure that $y+$ value is less than 1, the thickness of the first layer mesh of blade, hub, and shroud is less than 0.01 mm. Based on the verification of mesh independence, shown in Fig. 15, the total number of nodes is determined to be 1.4 million.

Compared with the numerical simulation results, the experimental results are more accurate, but due to the limitation of experimental conditions, only few flow parameters can be acquired. The numerical simulation based on the RANS equations can obtain more detailed flow parameters, which can be utilized to verify whether the result of design is in line with expectations. It is necessary to confirm the accuracy of the numerical method by the experimental method for further. Therefore, the lift fan was manufactured, and the total thrust and torque at the design rotation speed were measured with an ATI-mini45 six-axis force/torque sensor as shown in Fig. 16.

The output shaft power is calculated by the motor performance curve and input electric power. PSI 9116 pressure scanning systems were used to measure the circumferential average static pressure distribution at different axial positions of the lift fan shroud surface, as shown in Fig. 17. Basic performance parameters obtained by the lifting line method, RANS and the experiment are shown in Table 3. The thrust is almost consistent with the expectation, and the torque of the rotor and stator are equalized as expected, and also the efficiency is high, close to 88.32%. It can be concluded that the results are mutually confirmed, excepting that the torque of R1 and S1 are underestimated. The error likely comes

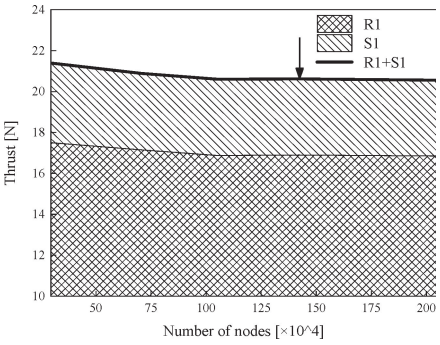


Fig. 15. Mesh independence verification.

©2022 JSASS

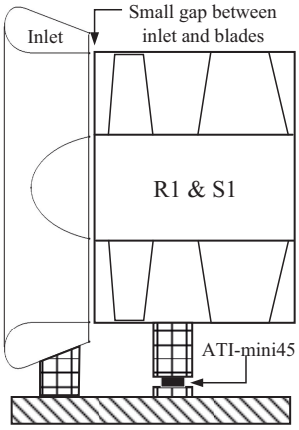


Fig. 16. Mechanical measurement of the lift fan.

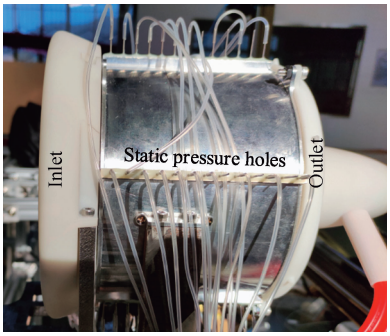


Fig. 17. Measurement of circumferential average static pressure at different axial positions of the shroud surface.

Table 3. Targets vs design results.

	Targets (Lifting line)	Results (RANS)	Results (EXP)
Total thrust (N)	20.0	20.4	19.8
R1 thrust (N)	16.79	16.76	—
S1 thrust (N)	3.26	3.67	—
R1 torque (N·m)	0.825	0.942	—
S1 torque (N·m)	−0.819	−0.922	—
Total torque (N·m)	0.006	0.020	0.024
Efficiency	—	90.97%	88.32%

from the tip clearance and viscosity which are not considered in the design process and the thin-airfoil experience model.

In flow details, Fig. 18 indicates that the shroud pressure distribution obtained by the numerical simulation method is also consistent with that obtained by experimental method, which proves the accuracy of the design and numerical method. Figure 19 shows the velocity contours of the rotor and stator blades at different sections. It can be seen that the matching between the blade profile and the flow field is reasonable in each section, and there is almost no flow separation phenomenon, excepting that the boundary layer at the suction side of blade root is thickened due to the combined effect of low speed and the viscosity of the hub. The flow field structure of the blade passage is consistent with the high efficiency shown by the numerical and experimental results.

It can be considered that results obtained by numerical simulation method has high accuracy through comparison

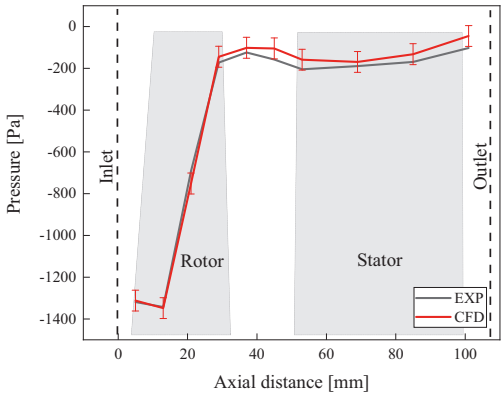


Fig. 18. Distribution of circumferential average static pressure at different axial positions of the shroud surface.

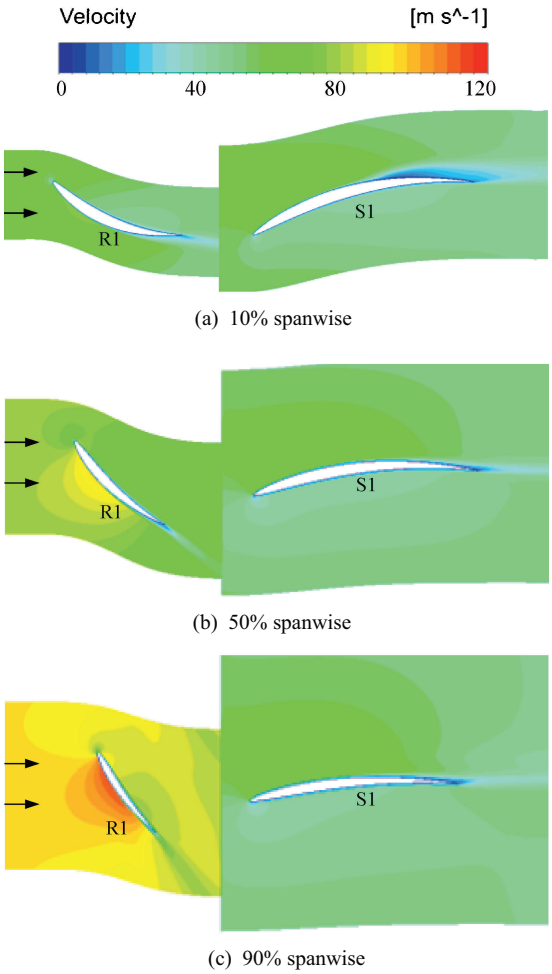


Fig. 19. Velocity contours at different spanwise.

with the experimental method, and then the CFD results will be used to verify the accuracy of the velocity distribution obtained by the lifting line method with the vortex rings correction, to rule out the contingency. Figure 20 shows the distribution of the axial induced velocity V_z predicted by the modified lifting line method in the R1 plane along with several span positions and its source of induced velocity. The results show that the axial induced velocity distribution is relatively uniform, which meets the design expectations. The

©2022 JSASS

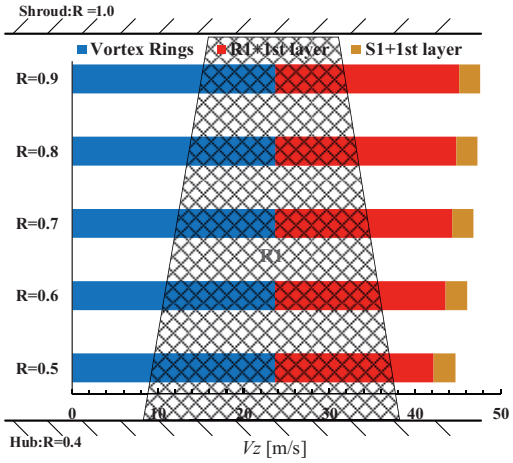


Fig. 20. Axial induced velocity distribution and composition in R1 plane.

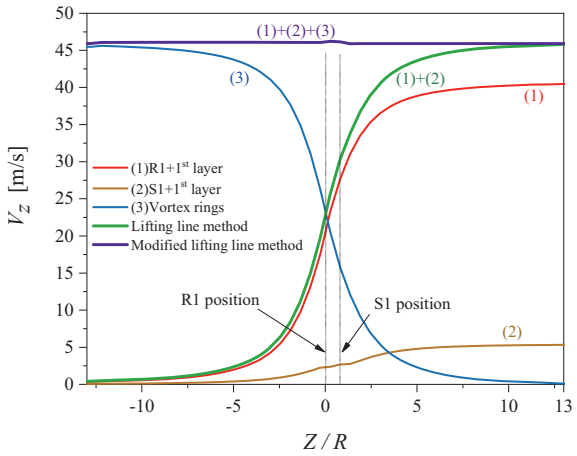


Fig. 21. Axial velocity distribution at different axial positions.

average axial induced velocity is about 46.3 m/s, which is still consistent with the RANS result (47.3 m/s). So far, it can be considered that two different methods have reached a unified conclusion on the macro level, which initially reflects the correctness of this modified lifting line method.

Figure 20 also shows the components of the axial induced velocity at the R1 plane. The induced velocity is mainly generated by the vortex rings and the semi-infinite wake vortex of R1. The axial position of R1 is located in the upstream of the semi-infinite wake vortex system of S1, so S1 has little contribution to the induced velocity. The large proportion of the induced velocity of the vortex rings in the total induced velocity initially reflects the importance and necessity of the vortex rings in establishing a reasonable flow field.

In order to confirm whether the flow field at different axial positions also conforms to the physical phenomenon in a straight duct with a constant area, the axial induced velocity and its components from inlet to outlet are provided in Fig. 21. The velocity from hub to shroud is fairly uniform as shown in Fig. 20, so the data at 50% spanwise are used to draw the axial velocity distribution from inlet to outlet.

The axial flow direction is defined along the Z-axis. The coordinate is dimensionless with rotor diameter (R) as reference. $Z = 0R$ is defined as the position of the rotor, the stator is at $Z = 0.8R$. The total axial velocity calculated by modified lifting line method in the duct is purple line which is composed by R1 horseshoe vortices and its first layer image vortices (1), S1 horseshoe vortices and its first layer image vortices (2) and vortex rings (3) as shown in Fig. 21. The velocity from inlet to outlet is almost unchanged, which is consistent with the law of velocity variation along the straight duct with constant area.

From the details, there are significant differences in the components of induced axial velocity at different axial positions. The axial velocity at the upstream is entirely induced by vortex rings which contribute for about 100%. The horseshoe vortices of the rotor and the stator are far away from this position and hardly contribute to the induced velocity. The axial velocity at the rotor is mainly induced by the semi-infinite horseshoe vortices of the rotor itself and the vortex rings, accounting for 43% and 50% respectively. The contribution of the semi-infinite horseshoe vortices of the stator to the induced velocity at the rotor begins to appear, but accounting for only 7% of total induced velocity. The stator is inside the semi-infinite horseshoe vortices of the rotor, so the axial induction of rotor horseshoe vortices is further enhanced, accounting for 59% of the total induced velocity, and the radial induced velocity is weakened. This phenomenon results in a decrease in the vortex rings intensity at a nearby position, and thus the induced velocity contribution of the vortex rings is further reduced to about 34%. The axial induced velocity at the downstream is almost induced by the rotor and stator. The effect of the semi-infinite horseshoe vortex has a high degree of similarity with that of infinite horseshoe vortex. Therefore, the radial induced velocity is almost zero, and the strength of the vortex rings tends to zero. The rotor as a rotating component has a horseshoe vortex pitch which is much smaller than that of the stator. Therefore, the contributor of the axial induced velocity at this position is mainly the horseshoe vortices of the rotor which accounting for 88%, and the horseshoe vortices of the stator which accounting for 12%. The variation of the composition of the induced velocity is consistent with the expectation, and the total velocity is consistent with the predicted results of RANS (47.3 m/s), which conforms to the velocity variation law along the straight duct with constant area.

If the wall effect is not corrected by vortex rings, the axial velocity distribution in the duct calculated by classical lifting line method with first layer image vortices is green line which is composed by (1) and (2) as shown in Fig. 21. Obviously, this is a nonphysical velocity distribution, and the axial induced velocity value at the rotor and stator position based on this result is clearly not available for blade design.

It can be concluded from the above analysis that the modified lifting line design method which is combined with the vortex rings has constructed the flow field induced by R1, S1 and duct accurately, and successfully used in the lift fan design.

©2022 JSASS

5. Conclusions

(1) For ducted fans with zero inflow, such as lift fans, the error of axial induced velocity directly constitutes all error of total axial velocity. Based on the image vortex method, it is difficult to predict the influence of the duct surface on the axial induced velocity, which leads to the failure of the original lifting line method.

(2) The vortex rings are added on original lifting line design method. By eliminating the normal induced velocity of the duct surface, the circulation distribution of the vortex rings is automatically obtained, and then the axial induced velocity come from the duct surface is corrected. Therefore, the application scope of the original lift line method is expanded, and it can be used for the design of lift fans even for zero inflow condition.

(3) Taking the lift fan as an example, the modified lifting line method is used for blade design, and the RANS method is used for verification. The results show that the designed geometry achieved the expected goal. Under the condition of zero inflow, the contribution of the vortex rings to the total axial induced velocity accounts for about 50%. It is further illustrated that the modified lifting line method which is combined with the vortex rings is reasonable and accurate.

(4) From the design results, there is a shortage of torque prediction due to the non-viscous assumption of the lifting line. It is necessary to add viscosity correction and BL (boundary layer) model to correct the viscous effect of blade, hub, and shroud in the future.

Acknowledgments

This work was supported by the Shenzhen Science and Technology Innovation Commission Project (JCYJ20170817110605193).

References

1) Ventura Diaz, P., Caracuel Rubio, R., and Yoon, S.: Simulations of Ducted and Coaxial Rotors for Air Taxi Operations, AIAA Aviation 2019 Forum, Dallas, Texas, 2019-2825, 2019.
2) Platt, R. J.: Static Tests of a Shrouded and an Unshrouded Propeller, NACA RM, No. L7H25, February, 1948.
3) Pereira, J. L. and Chopra, I.: Hover Tests of Micro Aerial Vehicle-scale Shrouded Rotors, Part I: Performance Characteristics, *J. Am. Helicopter Soc.*, **54**, 1 (2009), pp. 18–45.
4) Deng, S. and Ren, Z.: Experimental Study of a Ducted Contra-rotating Lift Fan for Vertical/short Takeoff and Landing Unmanned Aerial Vehicle Application, Proceedings of the Institution of Mechanical Engineers, Part G, *J. Aerosp. Eng.*, **232**, 16 (2018), 10.
5) Taylor, R. T.: Experimental Investigation of the Effects of Some Shroud Design Variables on the Static Thrust Characteristics of a Small-scale Shrouded Propeller Submerged in a Wing, Technical Report Archive & Image Library, Vol. 8, 1958, pp. 41–50.
6) Yilmaz, S., Erdem, D., and Kavsaoglu, M. S.: Performance of a Ducted Propeller Designed for UAV Applications at Zero Angle of Attack Flight: an Experimental Study, *Aerosp. Sci. Technol.*, **45** (2015), pp. 376–386.
7) Epps, B. P. and Kimball, R. W.: Unified Rotor Lifting Line Theory, *J. Ship Res.*, **57**, 4 (2013), pp. 181–201.
8) Saffman, P. G.: *Vortex Dynamics*, Cambridge University Press, London, Vol. 256, 1993, pp. 720–723.
9) Hsin, C.: Efficient Computational Methods for Multi-component Lifting Line Calculations, Master's Thesis, Massachusetts Institute of Technology, Department of Ocean Engineering, 1987.
10) Lerbs, H. W.: Moderately Loaded Propellers with a Finite Number of Blades and an Arbitrary Distribution of Circulation, *Trans. Soc. Naval Architects Marine Engineers*, **60** (1952), pp. 73–117.
11) Morgan, W. B. and Wrench, J. W.: *Some Computational Aspects of Propeller Design, Methods in Computational Physics*, Academic Press, Salt Lake City, 1965, pp. 301–331.
12) Wrench, J. W.: The Calculation of Propeller Induction Factors, DTMB Technical Report 1116, 1957.
13) Hough, G. R. and Ordway, D. E.: The Generalized Actuator Disk, Technical Report TAR-TR, 6401, Therm Advance Research, January 1964.
14) Hough, G. R. and Ordway, D. E.: Mean Flow Streamlines of a Finite-bladed Propeller, *J. Aircraft*, **4**, 6 (1971), pp. 561–562.
15) Epps, B.: On the Rotor Lifting Line Wake Model, *J. Ship Prod. Design*, **33**, 1 (2017), pp. 31–45.
16) Dickmann, H. E. and Weissinger, J.: Beitrag zur Theorie Optimaler Düsenschrauben (Kortdüsen), *Jahrb. Schiffbautechn.*, **49** (1955), pp. 253–305.
17) Drela, M. and Youngren, H.: XROTOR User Guide, Nov 13, 2003. http://web.mit.edu/drela/Public/web/xrotor/xrotor_doc.txt
18) Caster, E. B.: A Computer Program for Use in Designing Ducted Propellers, NSRDC Technical Report 2507, 1967.
19) Morgan, W. B. and Cast, E. B.: Prediction of the Aerodynamic Characteristics of Annular Airfoils, David Taylor Model Basin Report 1830, 1965.
20) Drela, M. and Youngren, H.: Axisymmetric Analysis and Design of Ducted Rotors, Dec 5, 2005. http://web.mit.edu/drela/Public/web/dfdc/DFDCtheory12-31.pdf
21) Kerwin, J. and Leopold, R.: Propeller-Incidence Correction Due to Blade Thickness, *J. Ship Res.*, **7**, 4 (1963), pp. 1–6.
22) Kerwin, J. and Hadler, J.: *Principles of Naval Architecture: Propulsion*, Society of Naval Architects and Marine Engineers, Jersey City, 2010, pp. 92–95.
23) Epps, B. P. and Kimball, R. W.: Unified Rotor Lifting Line Theory, *J. Ship Res.*, **57**, 4 (2013), pp. 181–201.
24) Houten, R. V.: Analysis of Ducted Propellers in Steady Flow, ARMC Report No. 4.76-1, 1986.
25) Coney, W. B.: A Method for the Design of a Class of Optimum Marine Propulsors, Ph.D. Thesis, Massachusetts Institute of Technology, 1989.
26) Wang, H., Wang, Y., and Deng, S.: Experimental Study of In-Ground-Effect on Force and Spectrum Characteristics of a Contra-Rotating Lift Fan, *J. Propul. Technol.*, **39**, 12 (2018), pp. 2703–2709.
27) Katz, J. and Plotkin, A.: *Low-Speed Aerodynamics*, Cambridge University Press, London, 2001, pp. 141–146.
28) Kuchemann, D. and Weber, J.: *Aerodynamics of Propulsion*, McGraw-Hill, New York, 1953, pp. 38–59.
29) Epps, B. P., Stanway, M. J., and Kimball, R. W.: OpenProp: An Open-source Design Tool for Propellers and Turbines, SNAME Propellers and Shafting, Williamsburg, 2009, DOI: 10.5957/PSS-2009-09.

Kwanjung Yee
Associate Editor

©2022 JSASS